ACS APPLIED MATERIALS & INTERFACES

Research Article

www.acsami.org

Exciton Generation/Dissociation/Charge-Transfer Enhancement in Inorganic/Organic Hybrid Solar Cells by Robust Single Nanocrystalline LnP_xO_y (Ln = Eu, Y) Doping

Xiao Jin,[†,∥] Weifu Sun,[‡,∥] Zihan Chen,[†] Taihuei Wei,[§] Chuyang Chen,[‡] Xingdao He,[†] Yongbiao Yuan,[†] Yue Li,[†] and Qinghua Li*[,†]

[†]Key Laboratory of Nondestructive Testing, Ministry of Education, Nanchang Hangkong University, Nanchang 330063, People's Republic of China

[‡]School of Materials Science and Engineering, The University of New South Wales, Sydney, NSW 2052, Australia

[§]Department of Physics, National Chung-Cheng University, Chia-Yi 621, Taiwan, Republic of China

Supporting Information

ABSTRACT: Low-temperature solution-processed photovoltaics suffer from low efficiencies because of poor exciton or electron−hole transfer. Inorganic/organic hybrid solar cell, although still in its infancy, has attracted great interest thus far. One of the promising ways to enhance exciton dissociation or electron−hole transport is the doping of lanthanide phosphate ions. However, the underlying photophysical mechanism remains poorly understood. Herein, by applying femtosecond transient absorption spectroscopy, we successfully distinguished hot electron, less energetic electron, hole transport from electron−hole recombination. Concrete evidence has been provided that lanthanide phosphate doping improves the efficiency of both hot electron and "less energetic" electron transfers from donor to acceptor, but the hole transport almost remains unchanged. In particular, the hot electron transfer lifetime was shortened from 30.2 to 12.7 ps, that is, more than 60% faster than pure TiO_2 acceptor. Such improvement was ascribed to the facts that the conduction band (CB) edge energy level of TiO_2 has been elevated by 0.2 eV, while the valence band level almost remains unchanged, thus not only narrowing the energy offset between CB levels of TiO_2 and P3HT, but also meanwhile enlarging the band gap of TiO_2 itself that permits one to inhibit electron−hole recombination within TiO_2. Consequently, lanthanide phosphate doped TiO_2/P3HT bulk-heterojunction solar cell has been demonstrated to be a promising hybrid solar cell, and a notable power conversion efficiency of 2.91% is therefore attained. This work indicates that lanthanide compound ions can efficiently facilitate exciton generation, dissociation, and charge transport, thus enhancing photovoltaic performance.

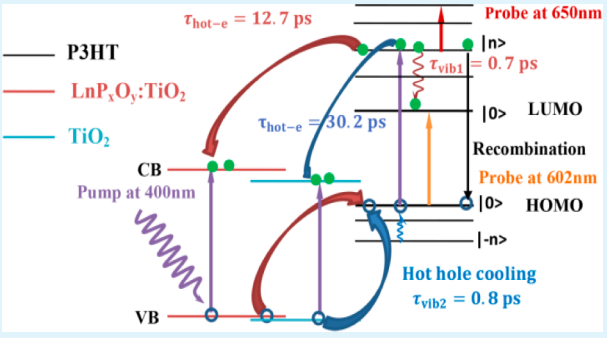

KEYWORDS: *inorganic/organic hybrid solar cell, charge photogeneration dynamics, energy band regulation, bulk-heterojunction*

1. INTRODUCTION

It is known that the current solar cell market is dominated by inorganic photovoltaic (PV) cells (e.g., silicon solar cell), whereas the emerging technologies such as dye-sensitized solar cell (DSSC)[1−4] and organic solar cell[5] (e.g., polymer solar cell) have also attracted interest. However, either inorganic or organic PV cell suffers from certain shortcomings, although each bears unique advantages. In detail, although both silicon[6] and dye-sensitized solar cells[7] have attained a solar-to-electric power conversion efficiency (PCE) of more than 10% milestone, nevertheless due to the expensive raw materials and fine processing[8] or due to the challenging long-term stability,[2,3] a desired and promising candidate of exploiting advantageous characteristics of both inorganic and organic semiconductors is still intensively pursued. Hitherto, although various kinds of hybrid solar cells (HSCs) such as hybrid Si−organic solar cells[9] and hybrid−DSSC devices[10] have been developed, nevertheless one should bear in mind that each of them inevitably bears the above-mentioned defects of either silicon or DSSC-based devices. Inorganic/organic HSCs, with a bulk-heterojunction (BHJ) architecture consisting of an organic conjugated polymer as the hole transporter and inorganic semiconductor as electron transporter in a photoactive layer, have attracted increasing attention and become of great interest to the researchers[11−15] due to the promising potentials of exploiting advantageous properties of both organic polymer and inorganic semiconductors, such as utilizing inexpensive and environmentally compatible raw materials[16,17] and a facile

Received: March 16, 2014
Accepted: May 16, 2014
Published: May 16, 2014

   dx.doi.org/10.1021/am501597k | ACS Appl. Mater. Interfaces 2014, 6, 8771−8781

solution-processed manufacturing to enable potentially low-cost solar cells.[18−20]

Despite the advantages exhibited by inorganic/organic HSCs, as a relatively newly emerging hotspot, to attain a desirable efficiency of solar cells based on inorganic nanoparticles and a well-known conducting polymer poly(3-hexylthiophene) (P3HT) BHJ remains challenging and still in its infancy. Over the last five years, most of the reported PCE of solar cells based on P3HT is around 2%, ranging from 1.7−2.6%, depending on the type of inorganic nanocrystals (except quantum dots, which are more related to colloidal quantum dot solar cells[21]), organic morphology,[22,23] and others.[8,24] Whereas titanium dioxide (TiO_2) is widely recognized as the most promising and versatile photocatalyst due to its outstanding physical and chemical properties including photostability, nontoxicity, inexpensiveness, and appropriate electronic band structure, thus TiO_2−P3HT holds great promise in pursuing efficient and inexpensive HSCs. It is also known that the high efficiency is critically dependent on the efficient exciton generation, dissociation, the transfer of charges, and less charge carrier recombination.[25] However, the energetic charges that are produced by the photon absorption of P3HT, that is, electron−hole pairs, are tightly bound by the strong Coulomb attraction, thus adding difficulties to the efficient charge separation and limiting the improvement of the PCE.[26−28] The highest occupied molecular orbital (HOMO) and lowest unoccupied molecular orbital (LUMO) edges of P3HT are at −5.1 and −3.0 eV, respectively, as compared to −7.4 and −4.2 eV versus vacuum for valence band (VB) maximum and conduction band (CB) minimum of TiO_2, respectively. The energy offset between the LUMO energy level of donor (P3HT) and CB edge of acceptor (TiO_2) is ∼1.2 eV, which enables one to break the Coulomb attraction (typically 0.1−0.5 eV) but not in an efficient way.[29] Because there was a larger energy offset at the donor/acceptor interface, there was a longer transfer time from donor to acceptor. Thus, an efficient energy transduction not only requires the separation of the photogenerated electron−hole pairs into long-lived dissociated charges with a minimal loss of free energy, but also requires an appropriate energy offset that enables the efficient charge transfer. The ability of a semiconductor to undergo photo-induced electron transfer to inorganic adsorbed acceptor is governed by the energy band positions of the semiconductor.[30] Therefore, to regulate the energy positions of conduction and valence bands of the acceptor is a promising approach to decrease the energy offset and finally improve the efficiency of HSCs.[31−33]

The intensively pursued nanocrystalline rare-earth phosphates, which can broaden the absorption domain to enhance the exciton generation and improve the transfer of charges by the doping effects,[34−36] have attracted significant attention due to their intrinsic and unique conversion properties.[37] Especially, europium or yttrium ion has demonstrated an excellent enchancement of ultraviolet light harvesting via a down-conversion luminescence process in DSSC devices.[38−40] With such benefits of rare earth ions, we envision that rare earth ions should also be critical to inorganic/organic HSCs because the solution-processed light-harvesting films prepared by techniques such as bath soaking are typically amorphous or polycrystalline,[41,42] consequently suffering from the poor charge-carrier transport. Nonetheless, little significant research on the doping effect induced by lanthanide phosphates in the inorganic/organic HSCs has been attempted thus far. Also, the crucial role of regulating energy band positions is not clarified, and charge photogeneration dynamics, the innate dynamics of the photoexcited electrons and holes driving the high efficiency of HSCs by lanthanide phosphates, have not been explored yet, although the conversion properties of lanthanide rare-earth materials have been demonstrated in previous work.[38−40]

Herein, the dual functions of lanthanide phosphates acting to widen the absorption range of P3HT and regulate energy band positions of TiO_2 are confirmed by the photoluminescence (PL) spectrum and cyclic voltammetry (CV) characteristic. To elucidate the origin of the efficiency improvement, by applying pump−probe spectroscopy and femtosecond transient absorption spectroscopy, we successfully monitored the electron dynamics, hole dynamics, and electron−hole recombination. Also, concrete evidence has been provided that both the hot electron and the less energetic electron transfers at the interface from donor to acceptor have been improved. A novel BHJ solar cell based on lanthanide phosphate doped TiO_2/P3HT was fabricated, and its photovoltaic characteristics were correspondingly examined.

2. EXPERIMENTAL SECTION

Materials. All chemical reagents including tetrabutyl titanate, poly(ethylene glycol) (PEG, molecular weight of 20 000), nitric acid, phosphoric acid, P25 (Degussa), OP emulsifying agent (Triton X-100), diammonium hydrogen phosphate, acetonitrile, isopropanol, yttrium oxide, and europium oxide are of analytic purity and were purchased from Sigma-Aldrich, Hongkong, China. Conjugated polymer P3HT and poly(3,4-ethylenedioxylenethiophene)-polystylene sulfonic acid (PEDOT:PSS) were provided by Aldrich. Fluorine-doped tin oxide glass (FTO, sheet resistance 8 Ω cm^{-2}) was purchased from Hartford Glass Co., U.S.

Preparation of LnP_xO_y. LnP_xO_y powder was prepared by the hydrothermal method.[43] First, Y_2O_3 (0.050 mol) and Eu_2O_3 (0.002 mol) were mixed and homogenized thoroughly. Next, adequate nitric acid was added into the mixture under heating and stirring. After being completely dissolved, the mixture was quickly transferred into a Teflon-lined stainless-steel autoclave, followed by adding $(NH_4)_2HPO_4$ (0.100 mol) into the autoclave under stirring. Afterward, appropriate deionized water was added until the filled degree reached 80% of the total container volume. The pH value of the mixed solution then was adjusted to 4 using phosphoric acid. The obtained solution was hydrothermally treated at 200 °C for 12 h. After being naturally cooled to room temperature, the obtained product was centrifuged, washed until the pH value of the system reached 7, and then dried in air at ambient temperature, followed by sintering in air at 850 °C for 30 min.

Synthesis of Lanthanide Phosphate Doped TiO_2. Lanthanide phosphate doped TiO_2 was prepared by the following procedure.[1,44] Tetrabutyl titanate (10 mL) was added to distilled water (100 mL) under stirring, followed by a white precipitate immediately. The precipitate was filtered, washed with distilled water, and then transferred to a mixed solution (150 mL) containing nitric acid (1 mL) and acetic acid (10 mL) at 80 °C. Under vigorous stirring, a light blue TiO_2 precursor was formed, followed by ultrasonic stirring for 30 min. Finally, the mixture was hydrothermally treated in an autoclave at 200 °C for 24 h to form a colloid of TiO_2. Subsequently, the P25 (0.075 g) and LnP_xO_y powder (0.375 g) were dispersed into the TiO_2 colloid by ultrasonically vibrating for 90 min and hydrothermally treating at 200 °C for 12 h to form a (TiO_2 + LnP_xO_y) colloid. At last, the resultant slurry was concentrated to 1/5 of its original volume by a thermal evaporation, and PEG-20000 (0.5 g) and a few drops of the Triton X-100 emulsifying agent were added. Finally, an even and stable TiO_2 colloid was produced.

Fabrication of HSC Devices. A layer of nanocrystalline lanthanide phosphate doped TiO_2 film with a thickness of 300 nm was prepared by coating the TiO_2 colloid on FTO glass using spin-coating

technique, followed by sintering in air at 450 °C for 30 min. The acceptor film then was soaked in a 0.15 mmol mL^{-1} P3HT toluene solution for 12 h to uptake P3HT. Next, PEDOT:PSS layer with a thickness of 50 nm was spin-coated onto the BHJ. Finally, about 50 nm thickness of Pt electrodes was deposited on the top of the PEDOT:PSS layer by thermal evaporation under vacuum. Note that the active area of the HSC device in this work is about 0.25 cm^2.

Characterizations. The phases of LnP_xO_y powder were identified by a Rigaku MiniFlex II X-ray diffractometer (XRD) using Cu Kα radiation (λ = 0.154 nm) at a power of 30 kV and 40 mA. The XRD patterns were collected in a scan mode at a scanning speed of 5° min^{-1} in the 2θ range between 15° and 80°. The microstructure of the LnP_xO_y powder was analyzed by means of high-resolution transmission electron microscopy (HR-TEM) and selected area electron diffraction (SAED), which were carried out by using a TEM (JEM-2010, JEOL Ltd.) working at 200 kV. Samples for TEM and HR-TEM characterizations were prepared by ultrasonically dispersing the LnP_xO_y powder in absolute ethanol, placing a small volume of this suspension on carbon-enhanced copper grids, and drying in air. The morphologies of the LnP_xO_y:TiO_2 layer and the cross-section of BHJ were characterized by using a field emission scanning electron microscope (FE-SEM, Hitachi S4800). The cyclic voltammetry (CV) characteristics were performed using a BAS 100B instrument at room temperature and a scan rate of 50 mV s^{-1} with tetrabutylammoniumhexafluorophosphate ($TBAPF_6$, 0.1 M) in acetonitrile as the supporting electrolyte, a platinized platinum (0.5 cm^2) as the counter electrodes, Ag/Ag^+ electrode as the reference electrode, and the TiO_2, LnP_xO_y:TiO_2, and LnP_xO_y films as work electrodes, respectively. The values are expressed in potentials versus F_c/F_c^+. Charge photogeneration dynamics of the BHJs were measured by the mode-locked Ti:sapphire laser (Coherent Mira 900) in combination with a regenerative amplifier (Coherent Legend-F). The photoluminescence spectrum was measured by using a spectrophotometer (FLS920, Edinburgh), in which a xenon lamp and a photomultiplier tube (R955, Hamamatsu) were used as excitation source and fluorescence detector, respectively. The photocurrent–voltage (J–V) curves of the assembled HSCs were recorded on an Electrochemical Workstation (Xe Lamp Oriel Sol_3A Class AAA Solar Simulators 94023A, U.S.) under an irradiation of a simulated solar light from a 100 W xenon arc lamp in ambient atmosphere.

Charge Photogeneration Dynamics. Time-resolved photoluminescence (PL) spectrum was measured on a spectrometer (Bruker Optics 250IS/SM) with intensified charge coupled device detector (Andor, IStar740). The samples were excited by 120 fs laser pulses at 400 nm with a repetition rate of 10 Hz. The time resolution of this experiment was determined to be ~60 ps. Femtosecond transient absorption spectrum was performed as follows: the ultrafast light source with a temporal resolution of ~120 fs was generated by a mode-locked titanium-sapphire laser operating at 800 nm. An optical parametric amplifier (OPA-800CF-1, Spectra Physics) provided the ultra-short laser pulses at desired wavelengths (~120 fs, full width at half maximum). A continuum white light generated from a sapphire plate was directed into the excited sample and detected by a charge coupled device (CCD) detector. Ultra-short laser pulses at 400 nm were employed as the pump light for the sample excitation and the probe light for the absorption measurement. Transient absorption at various delay times was measured by controlling the arrival time of each laser pulse at the sample. The laser system was operated at a repetition rate of 10 Hz; thus each pulse excited fully relaxed sample. Each datum was obtained by averaging 100 individual measurements to improve the signal-to-noise ratio, and the typical detection sensitivity of the difference aborption (ΔOD) was better than 10^{-4}.

3. RESULTS AND DISCUSSION

3.1. Characterization of Prepared LnP_xO_y Powder. In the present work, LnP_xO_y powder was first prepared by the hydrothermal method,[43] and then the lanthanide phosphate doped TiO_2 colloid was prepared as per the procedure reported.[1,44,45] The XRD patterns of LnP_xO_y powder are shown in Figure 1a. It reveals that the diffraction peaks can be

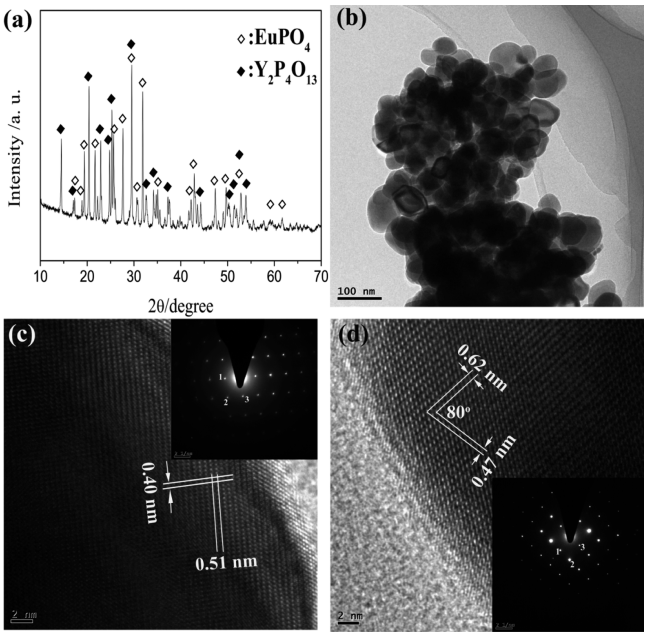

Figure 1. (a) XRD patterns of LnP_xO_y (Ln = Eu, Y) powder; (b) TEM image showing the morphology and the size of the generated powder with (c) and (d): HR-TEM images showing an individual nanocrystal. The insets are the corresponding SAED patterns of $EuPO_4$ crystal and $Y_2P_4O_{13}$.

indexed as those of the monoclinic phase of $EuPO_4$ nanocrystal and $Y_2P_4O_{13}$, which are consistent with the standard patterns of JCPDS25-1055, JCPDS35-0079, respectively. For example, the peaks at 17.282°, 22.161°, 27.533°, and 29.416° correspond to $(\bar{1},0,1)$, (1,0,1), (2,0,0), and $(\bar{1},2,0)$ planes of $EuPO_4$, respectively. Further structural characterizations of the powder were carried out by TEM. Figure 1b shows the TEM images of the prepared crystals, indicating that most of the crystals are in the nanometer domain. Figure 1c and d reveals the HR-TEM images and the corresponding SAED patterns of $EuPO_4$ crystal and $Y_2P_4O_{13}$, respectively. Figure 1c demonstrates that the values of distance spacing of d_1 = 0.519, d_2 = 0.327, and d_3 = 0.403 nm obtained from SAED are in agreement with those obtained from XRD pattern, that is, d_1 = 0.5127, d_2 = 0.3237, and d_3 = 0.4008 nm corresponding to $(\bar{1},0,1)$, (2,0,0), and (1,0,1) planes, respectively. Likewise, Figure 1d reveals that the values of d-spacing of d_1 = 0.472, d_2 = 0.347, and d_3 = 0.620 nm are in agreement with those obtained from the XRD pattern, that is, d_1 = 0.437, d_2 = 0.352, and d_3 = 0.617 nm (note that because JCPDS35-0079 does not mark the hkl planes, the corresponding planes are unknown). It is also noteworthy that the signal intensity of certain peaks of $EuPO_4$ seems strong, although the initial usage of Eu is only about 5 mol %. This may be because, on one hand, some postions of peaks of both $EuPO_4$ crystal and $Y_2P_4O_{13}$ are consistent, thus leading to a strengthened intensity; on the other hand, the ratio of Eu to Y element may relatively increase after complete reactions, to which some hints can be given from the corresponding energy dispersive spectrum (EDS) as shown in Figure S1 and Table S1 of the Supporting Information.

3.2. Down-Conversion of Eu^{3+}. It is known that an ideal solar cell material should bear good optical absorption

characteristics first. The energy level diagram of Eu^{3+} excited at λ = 393 nm and a possible down-conversion mechanism is

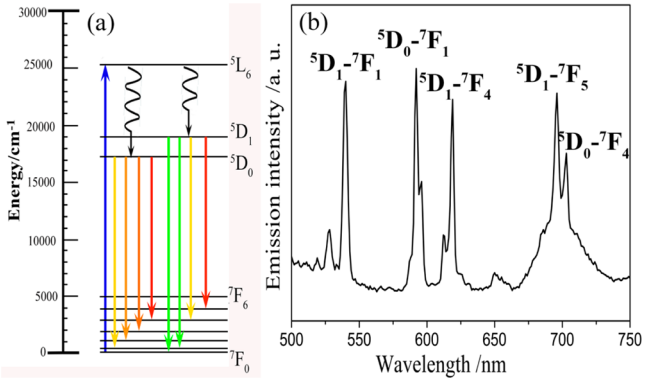

Figure 2. (a) Energy level diagram of trivalent Eu^{3+} ions with dominant visible emission transitions designated by arrows representing the approximate color of the fluorescence. (b) Fluorescence emission spectrum of LnP_xO_y excited at 393 nm.

shown in Figure 2. Briefly, Eu^{3+} ions are first excited from the $^7F_0$ ground state to the $^5L_6$ state after absorbing one pumping photon of λ = 393 nm. Nonradiative, multi-phonon decay is then responsible for populating the $^5D_1$ and $^5D_0$ states. Figure 2b shows the photoluminescence spectra of LnP_xO_y excited in the $^5L_6$ ($^7F_0 \rightarrow {}^5L_6$) of Eu^{3+} at 393 nm, followed by the emission of Eu^{3+} in the visible light range. The emission spectrum of LnP_xO_y under 393 nm excitation consists of line peaks mainly located at 592, 612, 650, and 701 nm, corresponding to the transitions of Eu^{3+} ions, that is, $^5D_0 \rightarrow {}^7F_J$ (J = 1, 2, 3, 4).[46] In addition, the peaks at 527, 539, 618, 696 nm stem from the transitions of Eu^{3+} ions: $^5D_1 \rightarrow {}^7F_0$, $^5D_1 \rightarrow {}^7F_1$, $^5D_1 \rightarrow {}^7F_4$, and $^5D_1 \rightarrow {}^7F_5$, respectively. Therefore, the ultraviolet irradiation at 393 nm can be converted to the visible light and near infrared spectrum (500−750 nm) via down-conversion luminescence of Eu^{3+}. Consequently, the light absorption range of P3HT is widened. Of note, the down-conversion of Eu^{3+} has been reported in the previous work associated with DSSC devices;[38] therefore, herein the fluorescence emission spectrum only was used to confirm this without using incident photon-to-current efficiency (IPCE) to further verify this.

3.3. Time-Resolved PL Decay Transients. As can be seen from Figure 3, all of the transient PL signals for the P3HT/methylbenzene solution, TiO_2/P3HT, and LnP_xO_y:TiO_2/P3HT films have prominent contributions from the electronic hyperpolarizability near zero delay, but exhibit a complicated temporal profile at positive time delay. We have decomposed the transient PL signals into three dynamically distinct components. These components include: (1) a slow component with an exponential time constant in the range ~nanosecond that accounts for the prominent shoulder in the upper curves of Figure 3b; (2) a fast decay, which accounts for the PL intensity at probe delays <100 ps; and (3) a response that is instantaneous on the time scale of the laser pulse and is well represented by a scalar multiple of the laser pulse autocorrelation function. Under the almost identical experimental conditions, the fast component of PL signal of the P3HT was greatly reduced when the P3HT is interfaced with an electron extracting TiO_2 layer or LnP_xO_y:TiO_2 layer. These

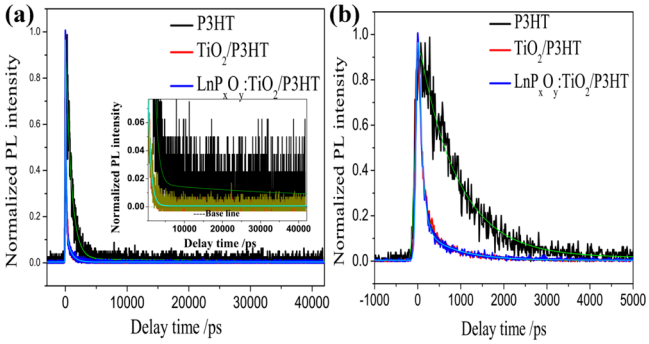

Figure 3. (a) The normalized time-resolved PL decay transients measured at 602 nm for P3HT/methylbenzene solution (black), TiO_2/P3HT (red), and LnP_xO_y:TiO_2/P3HT (blue) films after excitation at 400 nm (10 Hz, 30 ps, 4 mJ/cm^2). The solid lines are the double-exponential fits of the PL decay transients,[47] and the inset highlights the enlarged curves on long time scale. (b) The normalized time-resolved PL decay transients around zero delay.

high degrees of PL quenching indicate that there exists a strong charge transfer in these blended donor−acceptor system. Of note, the fast PL quenching is expected to originate from the hot electron transfer with a fitted lifetime of $\tau_{hot\text{-}e}$ = 892 to 80 ps, and the fluorescence decay time was estimated to be about τ_{flu} = 38 ± 12 ns (Supporting Information, Table S2). However, because of the limited temporal resolution of ~60 ps, our time-resolved PL decay transients cannot accurately reveal the effect of doping on the hot electron transfer, whose transfer time is on the order of picosecond.[29] What is more, because of the relatively poor signal to noise ratio (SNR), it cannot effectively monitor all of the photoexcited charge carriers including the hot electron, less energetic electron, and holes. Therefore, femtosecond transient absorption spectroscopy with a temporal resolution of ~120 fs and a high SNR (10^{-4}) was applied, and we successfully distinguished the hot electron, less energetic electron, hole transfers, and even electron−hole recombination.

3.4. Energy Diagram and the Dynamics of Electron and Hole Transport. Apart from the good optical absorption characteristics, an ideal solar cell material also should have efficient charge-transport properties. Thereby, femtosecond time-resolved absorption spectroscopy was adopted to explore the primary dynamics of photogenerated charges and to probe the role of the energy level regulation induced by LnP_xO_y (Ln = Eu,Y), which have seldom been detailed before. The CV characteristics show that the doping of LnP_xO_y results in the changes of the energy positions of CB and VB of acceptor TiO_2: the CB energy level of TiO_2 has changed from −0.38 to −0.58 eV (vs Ag/Ag$^+$), while the VB energy level almost does not change, lowered by 0.05 eV only (Supporting Information, Figure S2 and Table S3). Now one will wonder what influence it will exert on the primary dynamics of the photoexcited electrons and holes in the LnP_xO_y:TiO_2/P3HT BHJ, that is, the transport of electron/hole at the interface of acceptor and donor. Heterogeneous electron transfer in solar cells has been probed using transient absorption spectroscopy;[47,49] nevertheless, extending this approach to LnP_xO_y:TiO_2/P3HT film remains challenging due to the scattering effect of TiO_2 substrate, limited delay time, and temporal resolution. In our experiment, the effect of scattering stemming from TiO_2 substrate has been overcome, and a wider delay time from −5 ps to 2.5 ns and a higher temporal resolution of ~120 fs was

employed, thus allowing us to simultaneously examine the primary dynamics of both electron/hole transfer (on the picosecond time scale) and electron−hole recombination (on the nanosecond time scale).

The energy-band model shown in Figure 4 interprets the optical excitation and subsequent relaxation process. Each band

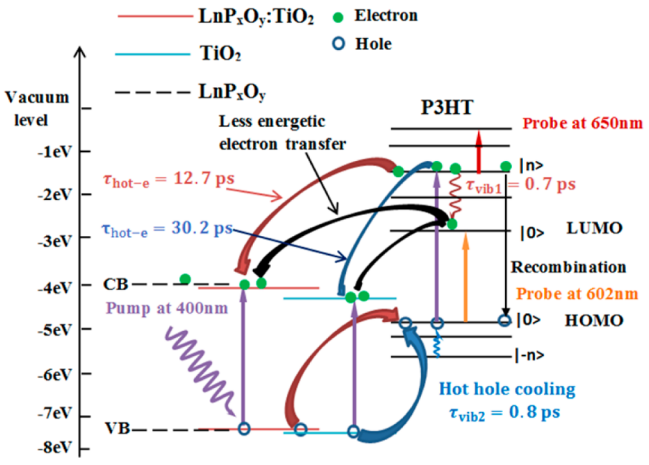

Figure 4. Energy level diagram of acceptor/donor showing optical excitation (up arrows), nonradiative relaxation (curved lines), radiative relaxation (down arrows), and electron−hole transfer times. $|n\rangle$ refers to the vibrational eigenstates involved in transitions. Violet up-arrow denotes the excitation to form electron−hole pairs, and curved lines mark the vibrational relaxation (the red curved line represents the cooling of hot electrons τ_{vib1}, while the blue line denotes the cooling of hot holes τ_{vib2}). The HOMO and LUMO energy levels of P3HT are −5.1 and −3.0 eV, respectively.[48]

(including the associated vibronic level $|v\rangle$) of P3HT molecules is conventionally denoted as S^m_{P3HT} for the singlet manifold, where the superscript refers to the state formed from certain electronic configurations in molecular orbitals. The VB and CB energy levels of LnP_xO_y:TiO_2 are referred as $S^0_{acceptor}$ and $S^1_{acceptor}$, respectively. The transitions from the singlet to the triplet of P3HT are not our concern because of the long intersystem crossing time (hundreds of nanoseconds). At the thermal equilibrium, the unperturbed P3HT molecules reside in the ground state S^0_{P3HT}. When pumped by a laser pulse at 400 nm, the molecules were promoted to a vibronic level of P3HT $S^1_{P3HT}|n\rangle$ via a one-photon process, that is, charge generation[29] (Figure 3, violet up-arrows in P3HT). The molecules were first excited to a vibronic level of S^1_{P3HT}, and then the separated hot electrons undergo one of the following processes: (a) the cooling via a vibronic relaxation to a lower vibronic level of P3HT S^1_{P3HT} $|0\rangle$ (Figure 3, red curved lines in P3HT) with a decay lifetime of τ_{vib1} in sub-picosecond;[50] (b) the recombination with the hole excitons at the ground state of P3HT (S^0_{P3HT}) with a recombination time constant τ_{re} (Figure 3, black down-arrow in P3HT); and (c) the diffusion to the interface of BHJ $S^1_{P3HT}|n\rangle \rightarrow S^1_{TiO_2}$ with a hot electron transfer time constant $\tau_{hot\text{-}e}$ (Figure 4, brown down-arrow from donor to acceptor). The delocalized electron transfer comprises the hot electron transfer and "less energetic" electron transfer. The absorption of high-energy photons creates hot electrons and holes that cool quickly to the band edges. However, the energy dissolved from the fast decays was converted into the kinetic energy of the electrons in the order of sub-picosecond. The energy converting process occurs long before the subsequent energy dissipation into adjacent molecules because the correlative local thermoequilibrium time is on the hundreds of picosecond time scale. The electronic relaxation rate is known to increase exponentially.[51] Thus, the hot-electron transfer can compete with the cooling of hot electrons. Unfortunately, not all of the energetic electrons can inject into the CB level of the acceptor. A number of the hot electrons were cooled by the emission of phonons after hundreds of picosecond, and then the "less energetic" electron may transfer to the interface of BHJ. Because of the initial cooling process, a substantial amount of solar energy has already been irreversibly lost.[49]

The transient absorption spectrum (TAS) (580−700 nm) of donor/acceptor films excited by the 400 nm femtosecond laser pulse with a specific delay time from 0 to 500 ps is shown in Figure 5. The TAS consists of one negative and one positive

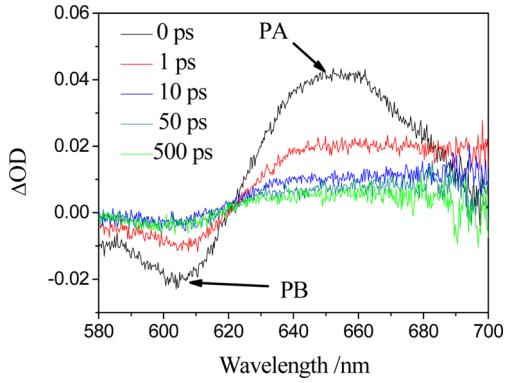

Figure 5. Transient absorption spectrum decays of LnP_xO_y:TiO_2/P3HT film excited at 400 nm, probed at 580−720 nm.

peak locating at ∼602, 650 nm, respectively. Note that the negative absorption bands at 602 nm are ascribed to the photobleaching (PB) of the ground-state absorption, which is consistent with the ultraviolet−visible absorption of P3HT (Supporting Information, Figure S2b). In contrast, the positive absorption peak at ∼650 nm was observed immediately after the laser excitation and is ascribed to the photoinduced excited-state absorption (PA). For 400 nm photoexcitation, it is reasonable to attribute the 650 nm PA band to the state-filling effects.[52−55] Additionally, it should be noted that both the negative and the positive peaks decay quickly from 0 to 50 ps, indicating that there exist fast mechanisms influencing PB and PA, and this agrees well with the time-resolved PL decay transients (Figure 3). However, on the longer time scale (50−500 ps), PA peaks decay slowly, whereas the PB peaks increase slightly, although not so obviously. The different characteristics of PA and PB signals are attributed to the complex electronic contributions such as charge generation, transfer, and recombination, which are disentangled below. Because the observed TAS signal has already been extensively discussed,[53−55] the transient absorption data that we observed may be taken as a convolution of the background-free laser pulse autocorrelation function $G(t)$ with the response function.[56,57]

$$S(\tau) = \int_{-\infty}^{+\infty} G(\tau - t)\phi(t)\,dt \quad (1)$$

The response function $\phi(t)$ may be taken to be a linear superposition of electronic contributions.

dx.doi.org/10.1021/am501597k | ACS Appl. Mater. Interfaces 2014, 6, 8771−8781

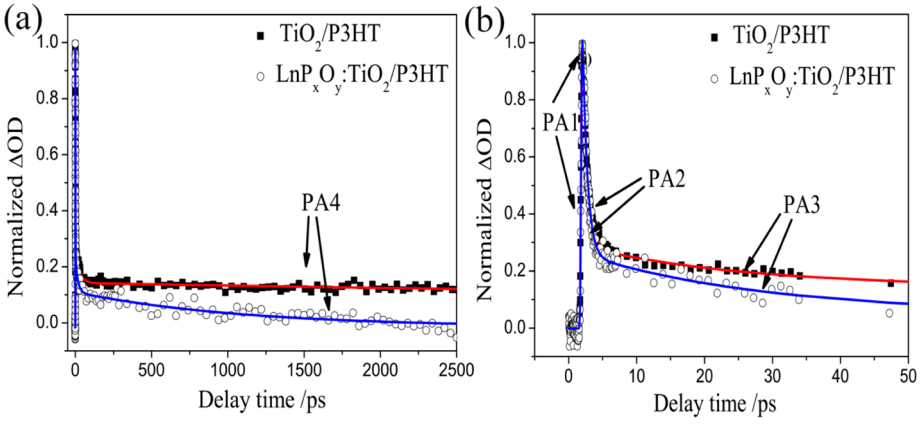

Figure 6. (a) Normalized femtosecond transient absorption decays of LnP_xO_y:TiO_2/P3HT (○) and TiO_2/P3HT (■) films excited at 400 nm (17 μJ cm^{-2}) probed at 650 nm. (b) The early time dynamics probed at 650 nm. The fitted hot electron transfer time constants with either LnP_xO_y:TiO_2/P3HT or TiO_2 as acceptor are $\tau_{hot\text{-}e}$ = 12.7 ± 1.6 ps, $\tau_{hot\text{-}e}$ = 30.2 ± 1.0 ps, respectively. The solid lines are the exponential fits using eq 2.

Table 1. Values for Lifetimes and the Amplitudes from Fits to Transient Absorption Decays Using the Linear Superposition of Electronic Contributions

lifetime (τ) (amplitude)	τ_{vib1}/ps (A)	$\tau_{hot\text{-}e}$/ps (B)	τ_{re}/ns (C)	τ_{vib2}/ps (D)	$\tau_{complex}$/ns (E)	τ_h/ns
LnP_xO_y:TiO_2/P3HT	0.73 ± 0.01 (0.91)	12.7 ± 1.6 (0.16)	11.0 ± 0.6 (0.13)	0.82 ± 0.04 (−0.80)	8.50 ± 1.00 (−0.19)	6.95 ± 0.35
TiO_2/P3HT	0.75 ± 0.01 (0.95)	30.2 ± 1.0 (0.15)	14.0 ± 1.5 (0.14)	0.80 ± 0.04 (−0.81)	8.50 ± 1.00 (−0.19)	6.95 ± 0.35

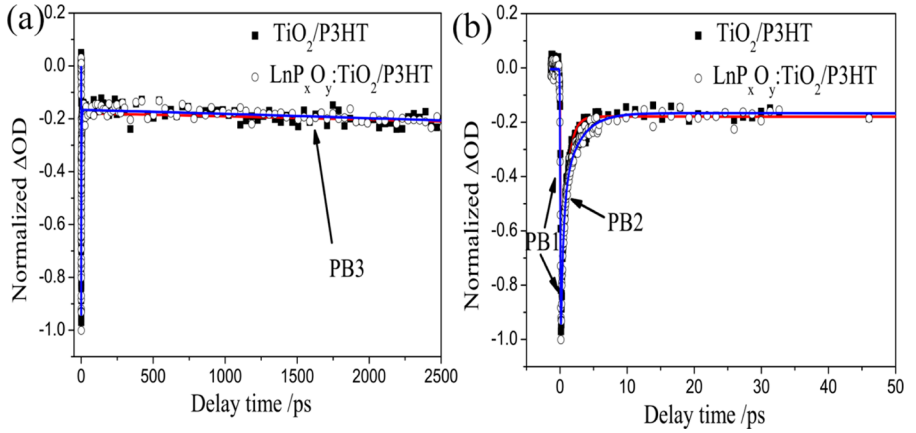

Figure 7. (a) Normalized femtosecond transient absorption decays of TiO_2/P3HT (■) and LnP_xO_y:TiO_2/P3HT (○) films excited at 400 nm (17 μJ cm^{-2}) probed at 602 nm. Solid lines are fitting curves with exponential components. (b) The early time dynamics probed at 602 nm. The hole transfer times of BHJs with LnP_xO_y:TiO_2 or TiO_2 as acceptor are identical, τ_h = 6.95 ± 0.35 ns.

3.5. Electron Transfer Dynamics. Next, we will detail the innate dynamics of the hot electron and the "less energetic" electron transfers. Comparative studies on the different acceptor/donor films at the identical probe wavelength with PA would yield detailed information about the charge-transfer dynamics including the electron transfer, hole transfer, and even electron−hole recombination, etc. The transient absorption dynamics at PA as shown in Figure 6 were used to inquire into the electron transport at the interface of acceptor/donor and the charge separation process. The complex state-filling effects can be regarded as the excited-state absorption from $S^1_{P3HT}|n\rangle$ to the higher levels with absorption cross section $\sigma_{S1} > \sigma_{S0}$. Thus, the PA decay monitors the variation of delocalized electron population of the excited state $S^1_{P3HT}|n\rangle$ in P3HT. We measured transient absorption decays probed at 650 nm to discuss the dynamics of singlet and the electron transport from donor to acceptor after the 400 nm excitation. The transient PA dynamics are described with a sum of three exponential functions:

$$\phi(t) = \delta(t) + A\exp(-t/\tau_{vib1}) + B\exp(-t/\tau_{hot\text{-}e}) + C\exp(-t/\tau_{re}) \quad (2)$$

where $\delta(t)$ is the pure electronic hyperpolarizability that responses instantaneously to the applied laser field (Figure 6, PA1), the second term is the nonradiatively decay from vibronic level $|n\rangle$ $|0\rangle$ of S^1_{P3HT} after excitation by the pump pulses (Figure 6, PA2), the third term is the intermolecular cross ($S^1_{P3HT}|n\rangle \rightarrow S^1_{acceptor}$) of the hot electron contributions to the detected signal (Figure 6, PA3), and the last term is the geminate recombination of electron−hole pairs (photoexcited electron−hole pairs that fail to fully dissociate) $S^1_{P3HT}|n\rangle \rightarrow S^1_{P3HT}$ responses (Figure 6, PA4). All of these decay transients were well fitted with three exponential time constants (Table 1). From fitting the normalized absorption decay dynamics with

energy-band model, with LnP_xO_y:TiO_2 layer present, we found that the hot electron transfer time was determined to be $\tau_{hot\text{-}e}$ = 12.7 ps and the hot electron transfer efficiency can be estimated as 13.3% by using the ratio of the amplitude $B/(A + B + C)$. However, with pure TiO_2 layer present, the hot electron transfer time and transfer efficiency can be estimated to be $\tau_{hot\text{-}e}$ = 30.2 ps and 12.1%, respectively. The variation of the hot electron transfer efficiency can be attributed to the energy level regulation induced by the doping of LnP_xO_y. With LnP_xO_y:TiO_2 as acceptor layer present, the hot electron transfer time from donor to acceptor was shortened, and the transfer efficiency was higher than that of pure TiO_2. Moreover, after doping with LnP_xO_y, the energy offset between the donor's LUMO and CB level of acceptor, that is, the CB-LUMO energy offset, narrows from 1.33 to 1.13 eV. However, the energy offset is still greater than the Coulomb binding energy (typically 0.1−0.5 eV), thus giving rise to an energetically downhill initial electron transfer. Those hot electrons that are excited by 400 nm pulses have considerable kinetic energy to cross the narrow energy offset of the interface into the acceptor $S^1_{P3HT}|n\rangle \rightarrow S^1_{acceptor}$. Yet the narrowing of energy offset still favors the hot electron transfer in a more efficient way, with less transfer time and hence less energy loss. It is also worth mentioning that the elevation of CB level of TiO_2 acceptor not only narrows the CB-LUMO energy offset, but also meanwhile enlarges the band gap of acceptor between its CB level and VB level, thus permitting one to inhibit or hamper the electron−hole recombination within acceptor itself. It is also noteworthy that the VB level of TiO_2 was lowered by 0.05 eV only, and almost remains unchanged (Supporting Information, Table S3).

As observed from Figure 6a, for both LnP_xO_y:TiO_2/P3HT and TiO_2/P3HT BHJs, the population of electron decreases with the increase in delay time, whereas according to the transient absorption dynamics of PB (Figure 7a), there is no decay of the hole in the VB level of P3HT on the long time scale (50 ps to 2.5 ns) either in TiO_2 or in LnP_xO_y:TiO_2 as acceptor present, and, on the contrary, the population of holes slightly increases with increase in delay time, although not so obviously. What is more, the electron−hole recombination times were determined to be τ_{re} = 11.0 and 14.0 ns, respectively, indicating that with LnP_xO_y:TiO_2 as acceptor, the delocalized electrons decay faster than that of pure TiO_2. On the basis of the conservation of particle number, the discrepancy of the electron−hole recombination time and the hole decay time can be attributed to the "less energetic" electron transfer from donor to acceptor. In other words, there exists another pathway for the electron relaxation. Those hot electrons in a vibronic energy level of excited state first relax to a lower vibronic energy level $S^1_{P3HT}|n\rangle \rightarrow S^1_{P3HT}|0\rangle$, and then may have enough time to transfer from donor to acceptor because of the long lifetime of geminate recombination (∼ns). Moreover, this electron transfer time can be estimated on the order of several nanoseconds because the recombination time is quenching from 14.0 to 11.0 ns. As the thermoequilibrium time is much shorter than this transfer time, the hot electron cooling process (subpicosecond) occurs long before transferring to the interface of heterojunction. Because of the initial cooling process, a lot of energy dissipates by the emission of phonons, and then those hot electrons develop into "less energetic" electrons.[49] The contribution of the less energetic electron transfer would mix with the recombination process. Moreover, the reduction of the electron−hole recombination time within donor implies a delay in the electron exhaustion and in turn favors the less energetic electron transfer from donor to acceptor. Thus, we conclude that the regulation of energy level by doping LnP_xO_y not only reduces the hot-electron transfer time, but also improves the less energetic electron transfer, and thus it is beneficial to the charge separation in BHJ.

3.6. Hole Transfer Dynamics. Because the transient PB decay can monitor the variation of the hole population of the ground S^0_{P3HT} in P3HT, we measured the PB decays at the probe wavelength of 602 nm thus to investigate the dynamics of the hole transfer from acceptor to donor.[52,54] The decay curves represent the change in the population of the hot holes in S^0_{P3HT}, which was excited by 400 nm pump pulse. There is no recovery of the hole population in the VB level of P3HT on the long time scale (50 ps to 2.5 ns) in either TiO_2 or LnP_xO_y:TiO_2. On the contrary, the population of holes slightly increases with the increase in delay time (Figure 7), despite the nonvanishing recombination time of the electron−hole pairs. Such increase of the hole population is attributed to the hole transport from the VB level of TiO_2:LnP_xO_y to the ground state of P3HT. In fact, under the excitation of 400 nm laser pulses, either TiO_2:LnP_xO_y or pure TiO_2 was also promoted to the CB ($S^1_{acceptor}$), and thus a large number of holes were formed in $S^0_{acceptor}$. Also, the hot holes in acceptor then may break the Coulomb attraction and cross to S^0_{P3HT}. However, when probed at 602 nm, the probe experienced the competition among the hot hole transports $S^0_{P3HT} \rightarrow S^0_{P3HT}$, the recombination of the electron−hole pairs $S^1_{P3HT} \rightarrow S^0_{P3HT}$, and the hole cooling by a lower vibrational relaxation $S^0_{P3HT}|-n\rangle \rightarrow |0\rangle$. As shown in Figure 7, the PB dynamics reveal that the population of holes increases in the time domain (50 ps to 2.5 ns) despite the recombination of the electron−hole pairs. This indicates that the hole transport $S^0_{TiO_2} \rightarrow S^0_{P3HT}$ dominates the contribution to the signal. Thus, transient PB of the ground-state absorption decay can be described with a sum of two exponential functions:

$$\phi(t) = \delta(t) + D\exp(-t/\tau_{vib2}) + E\exp(t/\tau_{complex}) \quad (3)$$

where the first term is the purely electronic hyperpolarizability that responds instantaneously to the applied laser field (Figure 7, PB1), the second term is the nonradiatively decay from a lower vibronic level $|n\rangle \rightarrow |0\rangle$ of S^0_{P3HT} that induces the hot-hole cooling (Figure 7, PB2), and the third term represents the complex contributions of hole transport $S^0_{TiO_2} \rightarrow S^0_{P3HT}$ and recombination of the electron−hole pairs $S^1_{P3HT} \rightarrow S^0_{P3HT}$ to the detected signal (Figure 7, PB3). The hole transfer from acceptor (either TiO_2 or LnP_xO_y:TiO_2) to P3HT gives rise to the holes population, whereas the recombination with the electrons in excited states $S^1_{P3HT}|n\rangle$ (n = 0,1,2,3...) with an effective fluorescence decay time τ_{flu} and the hot hole cooling from the lower vibrational relaxation with a decay time constant τ_{vib2} both give negative contributions to the population of holes. There exists a competition between the generation of new holes and the quenching; thus the hole transfer time τ_h can be estimated by using the relation $1/\tau_{complex} = 1/\tau_h - 1/\tau_{flu}$.[52] From fitting the normalized absorption decay dynamics using eq 3, with either LnP_xO_y:TiO_2 or TiO_2 layer present, we found that the complex decay time was almost the same (8.5 ns). Assuming that the fluorescence decay time of P3HT remains unchanged, that is, τ_{flu} = 38 ± 12 ns as obtained from the fits to time-resolved PL decay transients in Figure 3, the hole transfer time should be equal (∼6.95 ± 0.35 ns). This indicates that the

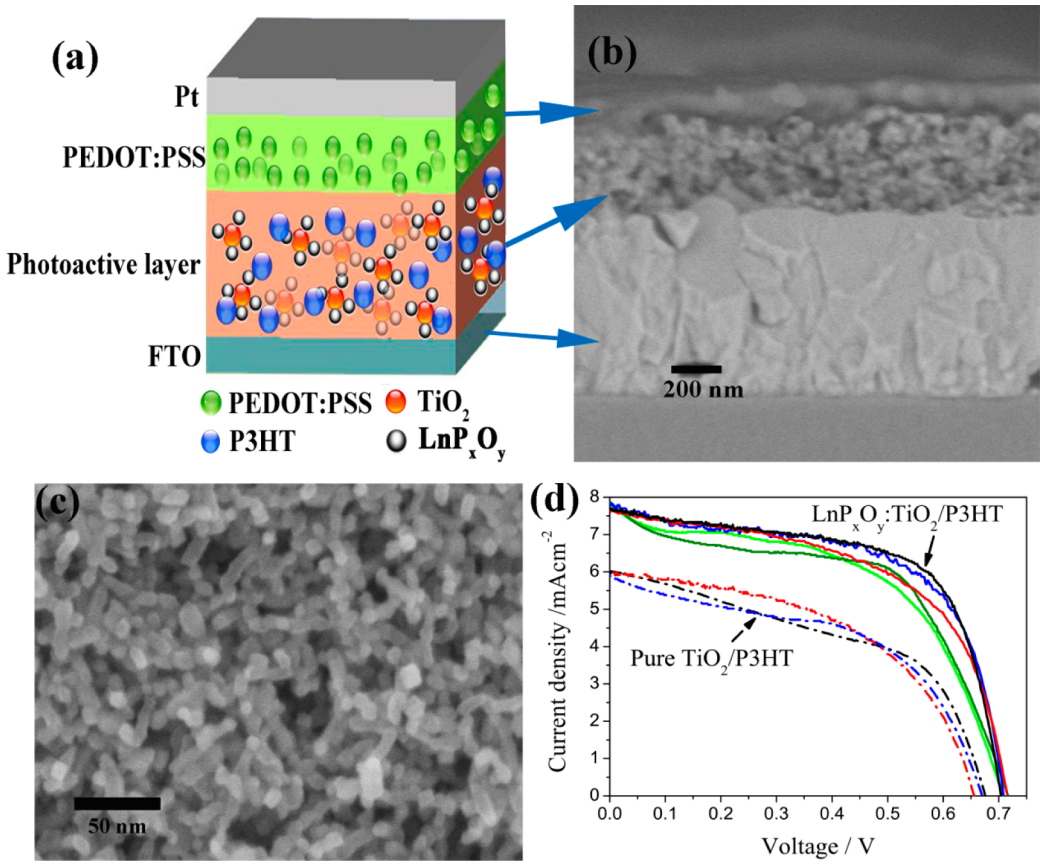

Figure 8. (a) Schematic diagram of the HSCs; (b) cross-sectional SEM image of the photovoltaic layer; (c) SEM image of porous TiO_2 layer; and (d) photocurrent–voltage characteristics of HSCs based on LnP_xO_y:TiO_2/P3HT (solid lines), and pure TiO_2/P3HT BHJs (dashed dotted lines), respectively.

Table 2. Photovoltaic Parameters of the HSCs Based on Different BHJs

BHJ	V_{oc} [V]	J_{sc} [mA cm^{-2}]	FF	η^a [%]
LnP_xO_y:TiO_2/P3HT	0.709 ± 0.005	7.73 ± 0.09	0.53 ± 0.01	2.91 ± 0.08
pure TiO_2/P3HT	0.667 ± 0.005	5.97 ± 0.06	0.50 ± 0.01	1.97 ± 0.02

$^a\eta = J_{sc}V_{oc}FF/P_{in}$, where P_{in} = 100 mW cm^{-2} (AM 1.5).

doping of LnP_xO_y gives little influence on the hole transport from acceptor to donor, which is in accordance with those obtained from the CV curves and PL spectra (Supporting Information, Figure S2 and Table S3). After doping LnP_xO_y, the CB energy levels of acceptors were affected largely, whereas the VB levels were only slightly affected. The results are in good agreement with the phenomenon that the complex decay times $\tau_{complex}$ of the different acceptors almost remain unchanged (Table 1).

3.7. Photovoltaic Performance of HSCs. With a view to exploring the doping effect of LnP_xO_y on the final photovoltaic performance, we prepared and characterized two types of films for comparison: pure TiO_2/P3HT and blended LnP_xO_y:TiO_2/P3HT films. Figure 8a schematically describes the architecture of the 3D LnP_xO_y:TiO_2/P3HT BHJ. The devices were fabricated by the sequential depositions of LnP_xO_y:TiO_2, P3HT, PEDOT:PSS, and Pt electrode on a transparent FTO substrate. The cross-section of the photovoltaic layer was characterized by SEM (Figure 8b): the different layers and their individual thickness of the FTO, BHJ, and PEDOT:PSS can be clearly distinguished. Especially, the thickness of the photovoltaic layer was estimated to be about 300 nm as observed from Figure 8b. In addition, the morphology of LnP_xO_y doped TiO_2 was characterized by SEM, and it can be observed from Figure 8c that the particle diameter of TiO_2 was estimated to be about 30 nm. The surface of the TiO_2 layer clearly exhibits a porous structure, which benefits the improvement of p–n contact for BHJ. On the other hand, the porous structure of TiO_2 layer[58] is ready for the adsorption of P3HT molecules by trapping the solution in the microporomerics.

Under the identical experimental conditions, the prepared HSCs with LnP_xO_y present deliver a notable efficiency of ~2.91%, enhanced by almost 48% as compared to its counterpart without LnP_xO_y doping (1.97%). This efficiency is higher than those of most of the other TiO_2/P3HT hybrid solar cells thus far.[8] The photocurrent–voltage (J–V) characteristics and photovoltaic parameters of the TiO_2/P3HT and LnP_xO_y:TiO_2/P3HT HSCs under a simulated solar light irradiation of 100 mW cm^{-2}, as shown in Figure 8d and Table 2, have improved after doping LnP_xO_y. In detail, the photocurrent density J_{sc} has increased from 5.97 to 7.73 mA cm^{-2}. Additionally, it is worth mentioning that the CB energy levels of acceptor are elevated by 0.2 eV while the energy levels of donor remain unchanged, which may provide some insight

into the slightly increased V_{oc} (from 0.667 to 0.709 V) according to eq S1 (Supporting Information).[59] This demonstrates that the doping of lanthanide phosphates indeed is critical to the photovoltaic performance of solar cells. Last, this work is initially motivated by exploring the potential powerful role lanthanide ions playing in inorganic/organic HSCs. However, having a better understanding of the underlying photophysical mechanism will shed some light on the designing rule of optimizing photovoltaic devices in future. Finally, due to the expensiveness of rare-earth materials and time-consuming processing techniques inherent in the present work, there still exists a gap from practical and commercial applications, which needs to be bridged in the future.

4. CONCLUSIONS

We have demonstrated that the incorporation of lanthanide phosphates into TiO_2 film indeed can result in an improvement of both the hot electron and the less energetic electron transfers at the interface of donor and acceptor, consequently enhancing photovoltaic performances. The underlying photophysical mechanism governing the double functions of down-conversion and energy band regulation was clearly unveiled by femtosecond transient absorption spectroscopy. Strikingly, the LnP_xO_y doping leads to an elevation of the CB level of TiO_2 by 0.2 eV (i.e., from −4.33 to −4.13 eV) while the VB level almost remains unchanged, and correspondingly the hot electron transfer time from donor to acceptor shortens by almost 60% (i.e., from $\tau_{hot\text{-}e}$ = 30.2 to 12.7 ps). Yet the hole transport from donor to acceptor almost remains unchanged, which matches well with the CV characteristic and PL spectra. Further, a novel hybrid LnP_xO_y doped TiO_2/P3HT BHJ that exploits the doping effect of lanthanide phosphate was engineered. The LnP_xO_y doped HSCs deliver a promising PCE of 2.91%, whereas a PCE of 1.97% was attained for its counterpart without incorporating lanthanide phosphate. Such high performance is ascribed to the down-conversion and the elevated CB level of acceptor, thereby enhancing exciton generation (via widening absorption range), promoting exciton dissociation by decreasing the energy offset between CB levels of donor and acceptor, and hence shortening intermolecular electron transfer time. This study opens a new direction toward the regulation of band position of acceptor, provides the promising potential of lanthanide dopants that have a crucial role in pursuing highly efficient HSCs to further enhance the efficiency, and also motivates the synthesis and development of more robust rare-earth compound for applications in solar cells.

■ ASSOCIATED CONTENT

Supporting Information

TEM and EDS analysis of the prepared powder, time-resolved PL decay transients, energy level regulations characterized by CV characteristics, and theory pertinent to open circuit voltage. This material is available free of charge via the Internet at http://pubs.acs.org.

■ AUTHOR INFORMATION

Corresponding Author

*Tel./fax: +86 791 86453203. E-mail: qhli@hqu.edu.cn.

Author Contributions

‖These authors contributed equally.

Notes

The authors declare no competing financial interest.

■ ACKNOWLEDGMENTS

We gratefully acknowledge the financial support of the Natural Science Foundation of China (61366003), the science and technology project of the education department of Jiangxi Province, China (GJJ12449, GJJ14533), and the Nanchang Hangkong University Doctor Program (EA201108333).

■ REFERENCES

(1) O'Regan, B.; Gratzel, M. A Low-Cost, High-Efficiency Solar Cell Based on Dye-Sensitized Colloidal TiO_2 Films. *Nature* **1991**, *353*, 737−740.

(2) Li, Q.; Wu, J.; Tang, Q.; Lan, Z.; Li, P.; Lin, J.; Fan, L. Application of Microporous Polyaniline Counter Electrode for Dye-Sensitized Solar Cells. *Electrochem. Commun.* **2008**, *10*, 1299−1302.

(3) Li, Q.; Chen, X.; Tang, Q.; Xu, H.; He, B.; Qin, Y. Imbibition of Polypyrrole into Three-Dimensional Poly(Hydroxyethyl Methacrylate/Glycerol) Gel Electrolyte for Robust Quasi-Solid-State Dye-Sensitized Solar Cells. *J. Mater. Chem. A* **2013**, *1*, 8055−8060.

(4) Wu, J.; Li, Y.; Tang, Q.; Yue, G.; Lin, J.; Huang, M.; Meng, L. Bifacial Dye-Sensitized Solar Cells: A Strategy to Enhance Overall Efficiency Based on Transparent Polyaniline Electrode. *Sci. Rep.* **2014**, *4*, 4028.

(5) Halls, J. J. M.; Walsh, C. A.; Greenham, N. C.; Marseglia, E. A.; Friend, R. H.; Moratti, S. C.; Holmes, A. B. Efficient Photodiodes from Interpenetrating Polymer Networks. *Nature* **1995**, *376*, 498−500.

(6) Wang, H.-P.; Lin, T.-Y.; Hsu, C.-W.; Tsai, M.-L.; Huang, C.-H.; Wei, W.-R.; Huang, M.-Y.; Chien, Y.-J.; Yang, P.-C.; Liu, C.-W.; Chou, L.-J.; He, J.-H. Realizing High-Efficiency Omnidirectional N-Type Si Solar Cells Via the Hierarchical Architecture Concept with Radial Junctions. *ACS Nano* **2013**, *7*, 9325−9335.

(7) Yella, A.; Lee, H.-W.; Tsao, H. N.; Yi, C.; Chandiran, A. K.; Nazeeruddin, M. K.; Diau, E. W.-G.; Yeh, C.-Y.; Zakeeruddin, S. M.; Grätzel, M. Porphyrin-Sensitized Solar Cells with Cobalt (II/III)−Based Redox Electrolyte Exceed 12 Percent Efficiency. *Science* **2011**, *334*, 629−634.

(8) Gao, F.; Ren, S.; Wang, J. The Renaissance of Hybrid Solar Cells: Progresses, Challenges, and Perspectives. *Energy Environ. Sci.* **2013**, *6*, 2020−2040.

(9) Huang, C.-Y.; Wang, D.-Y.; Wang, C.-H.; Chen, Y.-T.; Wang, Y.-T.; Jiang, Y.-T.; Yang, Y.-J.; Chen, C.-C.; Chen, Y.-F. Efficient Light Harvesting by Photon Downconversion and Light Trapping in Hybrid ZnS Nanoparticles/Si Nanotips Solar Cells. *ACS Nano* **2010**, *4*, 5849−5854.

(10) Choi, H.; Nicolaescu, R.; Paek, S.; Ko, J.; Kamat, P. V. Supersensitization of Cds Quantum Dots with a near-Infrared Organic Dye: Toward the Design of Panchromatic Hybrid-Sensitized Solar Cells. *ACS Nano* **2011**, *5*, 9238−9245.

(11) Zhao, L.; Lin, Z. Crafting Semiconductor Organic−Inorganic Nanocomposites via Placing Conjugated Polymers in Intimate Contact with Nanocrystals for Hybrid Solar Cells. *Adv. Mater.* **2012**, *24*, 4353−4368.

(12) Chen, Z.; Zhang, H.; Yu, W.; Li, Z.; Hou, J.; Wei, H.; Yang, B. Inverted Hybrid Solar Cells from Aqueous Materials with a PCE of 3.61%. *Adv. Energy Mater.* **2013**, *3*, 433−437.

(13) Gur, I.; Fromer, N. A.; Chen, C.-P.; Kanaras, A. G.; Alivisatos, A. P. Hybrid Solar Cells with Prescribed Nanoscale Morphologies Based on Hyperbranched Semiconductor Nanocrystals. *Nano Lett.* **2006**, *7*, 409−414.

(14) Sung, Y.-H.; Liao, W.-P.; Chen, D.-W.; Wu, C.-T.; Chang, G.-J.; Wu, J.-J. Room-Temperature Tailoring of Vertical ZnO Nanoarchitecture Morphology for Efficient Hybrid Polymer Solar Cells. *Adv. Funct. Mater.* **2012**, *22*, 3808−3814.

(15) Lee, J.; Mubeen, S.; Hernandez-Sosa, G.; Sun, Y.; Toma, F. M.; Stucky, G. D.; Moskovits, M. High-Efficiency Panchromatic Hybrid Schottky Solar Cells. *Adv. Mater.* **2013**, *25*, 256−260.

(16) Darling, S. B.; You, F. The Case for Organic Photovoltaics. *RSC Adv.* **2013**, *3*, 17633−17648.

(17) Darling, S. B.; You, F.; Veselka, T.; Velosa, A. Assumptions and the Levelized Cost of Energy for Photovoltaics. *Energy Environ. Sci.* **2011**, *4*, 3133−3139.
(18) Krebs, F. C.; Gevorgyan, S. A.; Alstrup, J. A Roll-to-Roll Process to Flexible Polymer Solar Cells: Model Studies, Manufacture and Operational Stability Studies. *J. Mater. Chem.* **2009**, *19*, 5442−5451.
(19) Krebs, F. C.; Jørgensen, M.; Norrman, K.; Hagemann, O.; Alstrup, J.; Nielsen, T. D.; Fyenbo, J.; Larsen, K.; Kristensen, J. A Complete Process for Production of Flexible Large Area Polymer Solar Cells Entirely Using Screen Printing—First Public Demonstration. *Sol. Energy Mater. Sol. Cells* **2009**, *93*, 422−441.
(20) Reeja-Jayan, B.; Manthiram, A. Influence of Polymer−Metal Interface on the Photovoltaic Properties and Long-Term Stability of nc-TiO_2-P3HT Hybrid Solar Cells. *Sol. Energy Mater. Sol. Cells* **2010**, *94*, 907−914.
(21) Maraghechi, P.; Labelle, A. J.; Kirmani, A. R.; Lan, X.; Adachi, M. M.; Thon, S. M.; Hoogland, S.; Lee, A.; Ning, Z.; Fischer, A.; Amassian, A.; Sargent, E. H. The Donor−Supply Electrode Enhances Performance in Colloidal Quantum Dot Solar Cells. *ACS Nano* **2013**, *7*, 6111−6116.
(22) Darling, S. B. Block Copolymers for Photovoltaics. *Energy Environ. Chem.* **2009**, *2*, 1266−1273.
(23) Chen, W.; Nikiforov, M. P.; Darling, S. B. Morphology Characterization in Organic and Hybrid Solar Cells. *Energy Environ. Sci.* **2012**, *5*, 8045.
(24) He, B.; Meng, X.; Tang, Q. Low-Cost Counter Electrodes from Copt Alloys for Efficient Dye-Sensitized Solar Cells. *ACS Appl. Mater. Interfaces* **2014**, *6*, 4812−4818.
(25) He, B.; Tang, Q.; Luo, J.; Li, Q.; Chen, X.; Cai, H. Rapid Charge-Transfer in Polypyrrole−Single Wall Carbon Nanotube Complex Counter Electrodes: Improved Photovoltaic Performances of Dye-Sensitized Solar Cells. *J. Power Sources* **2014**, *256*, 170−177.
(26) Ren, S.; Chang, L.-Y.; Lim, S.-K.; Zhao, J.; Smith, M.; Zhao, N.; Bulović, V.; Bawendi, M.; Gradečak, S. Inorganic−Organic Hybrid Solar Cell: Bridging Quantum Dots to Conjugated Polymer Nanowires. *Nano Lett.* **2011**, *11*, 3998−4002.
(27) Yu, G.; Heeger, A. J. Charge Separation and Photovoltaic Conversion in Polymer Composites with Internal Donor/Acceptor Heterojunctions. *J. Appl. Phys.* **1995**, *78*, 4510−4515.
(28) Huynh, W. U.; Dittmer, J. J.; Alivisatos, A. P. Hybrid Nanorod-Polymer Solar Cells. *Science* **2002**, *295*, 2425−2427.
(29) Ohkita, H.; Ito, S. Transient Absorption Spectroscopy of Polymer-Based Thin-Film Solar Cells. *Polymer* **2011**, *52*, 4397−4417.
(30) Clarke, T. M.; Durrant, J. R. Charge Photogeneration in Organic Solar Cells. *Chem. Rev.* **2010**, *110*, 6736−6767.
(31) Chen, L.-M.; Hong, Z.; Li, G.; Yang, Y. Recent Progress in Polymer Solar Cells: Manipulation of Polymer: Fullerene Morphology and the Formation of Efficient Inverted Polymer Solar Cells. *Adv. Mater.* **2009**, *21*, 1434−1449.
(32) Kovalenko, M. V.; Scheele, M.; Talapin, D. V. Colloidal Nanocrystals with Molecular Metal Chalcogenide Surface Ligands. *Science* **2009**, *324*, 1417−1420.
(33) Coe-Sullivan, S.; Steckel, J. S.; Woo, W. K.; Bawendi, M. G.; Bulović, V. Large-Area Ordered Quantum-Dot Monolayers via Phase Separation During Spin-Casting. *Adv. Funct. Mater.* **2005**, *15*, 1117−1124.
(34) Scharber, M. C.; Mühlbacher, D.; Koppe, M.; Denk, P.; Waldauf, C.; Heeger, A. J.; Brabec, C. J. Design Rules for Donors in Bulk-Heterojunction Solar Cells—Towards 10% Energy-Conversion Efficiency. *Adv. Mater.* **2006**, *18*, 789−794.
(35) Brédas, J.-L.; Cornil, J.; Heeger, A. J. The Exciton Binding Energy in Luminescent Conjugated Polymers. *Adv. Mater.* **1996**, *8*, 447−452.
(36) Muntwiler, M.; Yang, Q.; Tisdale, W. A.; Zhu, X. Y. Coulomb Barrier for Charge Separation at an Organic Semiconductor Interface. *Phys. Rev. Lett.* **2008**, *101*, 196403.
(37) Guo, H.; Sun, S. Lanthanide-Doped Upconverting Phosphors for Bioassay and Therapy. *Nanoscale* **2012**, *4*, 6692−6706.
(38) Hafez, H.; Wu, J.; Lan, Z.; Li, Q.; Xie, G.; Lin, J.; Huang, M.; Huang, Y.; Abdel-Mottaleb, M. S. Enhancing the Photoelectrical Performance of Dye-Sensitized Solar Cells Using TiO_2:Eu^{3+} Nanorods. *Nanotechnology* **2010**, *21*, 415201.
(39) Zhao, J.-X.; Lu, X.-H.; Zheng, Y.-Z.; Bi, S.-Q.; Tao, X.; Chen, J.-F.; Zhou, W. Eu Doping for Hierarchical ZnO Nanocrystalline Aggregates Based Dye-Sensitized Solar Cell. *Electrochem. Commun.* **2013**, *32*, 14−17.
(40) Wu, J.; Wang, J.; Lin, J.; Xiao, Y.; Yue, G.; Huang, M.; Lan, Z.; Huang, Y.; Fan, L.; Yin, S.; Sato, T. Dual Functions of YF_3:Eu^{3+} for Improving Photovoltaic Performance of Dye-Sensitized Solar Cells. *Sci. Rep.* **2013**, *3*, 2058.
(41) Selinsky, R. S.; Ding, Q.; Faber, M. S.; Wright, J. C.; Jin, S. Quantum Dot Nanoscale Heterostructures for Solar Energy Conversion. *Chem. Soc. Rev.* **2013**, *42*, 2963−2985.
(42) Facchetti, A. Π-Conjugated Polymers for Organic Electronics and Photovoltaic Cell Applications. *Chem. Mater.* **2010**, *23*, 733−758.
(43) Wang, J.; Wu, J.; Lin, J.; Huang, M.; Huang, Y.; Lan, Z.; Xiao, Y.; Yue, G.; Yin, S.; Sato, T. Application of Y_2O_3:Er^{3+} Nanorods in Dye-Sensitized Solar Cells. *ChemSusChem* **2012**, *5*, 1307−1312.
(44) Wu, J.; Hao, S.; Lan, Z.; Lin, J.; Huang, M.; Huang, Y.; Li, P.; Yin, S.; Sato, T. An All-Solid-State Dye-Sensitized Solar Cell-Based Poly(N-Alkyl-4-Vinyl-Pyridine Iodide) Electrolyte with Efficiency of 5.64%. *J. Am. Chem. Soc.* **2008**, *130*, 11568−11569.
(45) Wu, J.; Hao, S.; Lin, J.; Huang, M.; Huang, Y.; Lan, Z.; Li, P. Crystal Morphology of Anatase Titania Nanocrystals Used in Dye-Sensitized Solar Cells. *Cryst. Growth Des.* **2007**, *8*, 247−252.
(46) Tao, F.; Wang, Z.; Yao, L.; Cai, W.; Li, X. Synthesis and Photoluminescence Properties of Truncated Octahedral Eu-Doped YF_3 Submicrocrystals or Nanocrystals. *J. Phys. Chem. C* **2007**, *111*, 3241−3245.
(47) Guo, J.; Ohkita, H.; Benten, H.; Ito, S. Near-Ir Femtosecond Transient Absorption Spectroscopy of Ultrafast Polaron and Triplet Exciton Formation in Polythiophene Films with Different Regioregularities. *J. Am. Chem. Soc.* **2009**, *131*, 16869−16880.
(48) Liu, Y.; Summers, M. A.; Edder, C.; Fréchet, J. M. J.; McGehee, M. D. Using Resonance Energy Transfer to Improve Exciton Harvesting in Organic-Inorganic Hybrid Photovoltaic Cells. *Adv. Mater.* **2005**, *17*, 2960−2964.
(49) Tisdale, W. A.; Williams, K. J.; Timp, B. A.; Norris, D. J.; Aydil, E. S.; Zhu, X. Y. Hot-Electron Transfer from Semiconductor Nanocrystals. *Science* **2010**, *328*, 1543−1547.
(50) Seilmeier, A.; Kaiser, W. In *Ultrashort Laser Pulses*; Kaiser, W., Ed.; Springer: Berlin, Heidelberg, 1993; Chapter 7, pp 279−317.
(51) Schaller, R. D.; Pietryga, J. M.; Goupalov, S. V.; Petruska, M. A.; Ivanov, S. A.; Klimov, V. I. Breaking the Phonon Bottleneck in Semiconductor Nanocrystals via Multiphonon Emission Induced by Intrinsic Nonadiabatic Interactions. *Phys. Rev. Lett.* **2005**, *95*, 196401.
(52) Xing, G.; Mathews, N.; Sun, S.; Lim, S. S.; Lam, Y. M.; Gratzel, M.; Mhaisalkar, S.; Sum, T. C. Long-Range Balanced Electron- and Hole-Transport Lengths in Organic-Inorganic $CH_3NH_3PbI_3$. *Science* **2013**, *342*, 344−347.
(53) Klimov, V. I. Spectral and Dynamical Properties of Multiexcitons in Semiconductor Nanocrystals. *Annu. Rev. Phys. Chem.* **2007**, *58*, 635−673.
(54) Stranks, S. D.; Eperon, G. E.; Grancini, G.; Menelaou, C.; Alcocer, M. J.; Leijtens, T.; Herz, L. M.; Petrozza, A.; Snaith, H. J. Electron-Hole Diffusion Lengths Exceeding 1 Micrometer in an Organometal Trihalide Perovskite Absorber. *Science* **2013**, *342*, 341−344.
(55) Bakulin, A. A.; Hummelen, J. C.; Pshenichnikov, M. S.; van Loosdrecht, P. H. M. Ultrafast Hole-Transfer Dynamics in Polymer/PCBM Bulk Heterojunctions. *Adv. Funct. Mater.* **2010**, *20*, 1653−1660.
(56) McMorrow, D.; Lotshaw, W. T. Intermolecular Dynamics in Acetonitrile Probed with Femtosecond Fourier-Transform Raman Spectroscopy. *J. Phys. Chem.* **1991**, *95*, 10395−10406.
(57) McMorrow, D.; Lotshaw, W. T.; Kenney-Wallace, G. A. Femtosecond Optical Kerr Studies on the Origin of the Nonlinear

Responses in Simple Liquids. *IEEE J. Quantum Electron.* **1988**, *24*, 443−454.
(58) He, B.; Tang, Q.; Wang, M.; Ma, C.; Yuan, S. Complexation of Polyaniline and Graphene for Efficient Counter Electrodes in Dye-Sensitized Solar Cells: Enhanced Charge Transfer Ability. *J. Power Sources* **2014**, *256*, 8−13.
(59) Kroon, R.; Lenes, M.; Hummelen, J. C.; Blom, P. W. M.; de Boer, B. Small Bandgap Polymers for Organic Solar Cells(Polymer Material Development in the Last 5 Years). *Polym. Rev.* **2008**, *48*, 531−582.